Mechanical Properties of Nanowires and Nanobelts

Zhong Lin Wang
Georgia Institute of Technology, Atlanta, Georgia, U.S.A.

INTRODUCTION

Because of the high size and structure selectivity of nanomaterials, their physical properties could be quite diverse, depending on their atomic-scale structure, size, and chemistry.[1] To maintain and utilize the basic and technological advantages offered by the size specificity and selectivity of the nanomaterials, there are three key challenges that we need to overcome for the future technological applications of nanomaterials. First, synthesis of size, morphology and structurally controlled nanomaterials, which are likely to have the precisely designed and controlled properties. Secondly, novel techniques for characterizing the properties of individual nanostructures and their collective properties.[2] This is essential for understanding the characteristics of the nanostructures. Finally, integration of nanomaterials with the existing technology is the most important step for their applications, especially in nanoscale electronics and optoelectronics.

Characterizing the mechanical properties of individual nanotubes/nanowires/nanobelt [called one-dimensional (1-D) nanostructure] is a challenge to many existing testing and measuring techniques because of the following constrains. First, the size (diameter and length) is rather small, prohibiting the applications of the well-established testing techniques. Tensile and creep testing require that the size of the sample be sufficiently large to be clamped rigidly by the sample holder without sliding. This is impossible for 1-D nanomaterials using conventional means. Secondly, the small size of the nanostructure makes their manipulation rather difficult, and specialized techniques are needed for picking up and installing individual nanostructure. Therefore new methods and methodologies must be developed to quantify the properties of individual nanostructure. The objective of this chapter is to introduce the theory and techniques that have developed for characterizing the mechanical properties of individual nanotubes/nanowires/nanobelt using in situ transmission electron microscopy (TEM).

DYNAMIC BENDING MODULUS BY ELECTRIC FIELD-INDUCED MECHANICAL RESONANCE

The main challenge for characterizing the mechanical behavior of a single nanostructure is its ultrasmall size that prohibits the application of conventional techniques. We first have to see the nanostructure and then measure its properties. TEM is a powerful tool for characterizing the atomic-scale structures of solid materials. A modern TEM is a versatile machine that not only can provide a real space resolution better than 0.2 nm but also can give a quantitative chemical and electronic analysis from a region as small as 1 nm. It is feasible to receive a full structure characterization from TEM. A powerful and unique approach could be developed if we can integrate the structural information of a nanostructure provided by TEM with the properties measured in situ from the same nanostructure.[3–5] This is a powerful technique that not only can provide the properties of an individual nanotube but also can give the structure of the nanotube through electron imaging and diffraction, providing an ideal technique for understanding the property–structure relationship. The objective of this section is to introduce this technique and its applications.

Experimental Method

To carry out the property measurement of a 1-D nanostructure, a specimen holder for a TEM was built for applying a voltage across a 1-D nanostructure and its counter electrode (Fig. 1).[4,6] In the area that is loading specimen in conventional TEM, an electromechanical system is built that allows not only the lateral movement of the tip, but also applying a voltage across the 1-D nanostructure with the counter electrode. This setup is similar to the integration of scanning probe technique with TEM. The static and dynamic properties of the 1-D nanostructures can be obtained by applying a controllable static and alternating electric field. The microstructure of the measured object can be fully characterized by electron imaging, diffraction, and chemical analysis techniques.

The 1-D nanostructure to be used for property measurements is directly imaged under TEM (Fig. 2), and electron diffraction patterns and images can be recorded from the 1-D nanostructure. The information provided by TEM directly reveals both the surface and the intrinsic structure of the 1-D nanostructure. This is a unique advantage over the SPM techniques. The distance from the 1-D nanostructure to the counter electrode is controllable. The typical dimensions of the 1-D nanostructures are 5–100 nm in diameter/width and lengths of
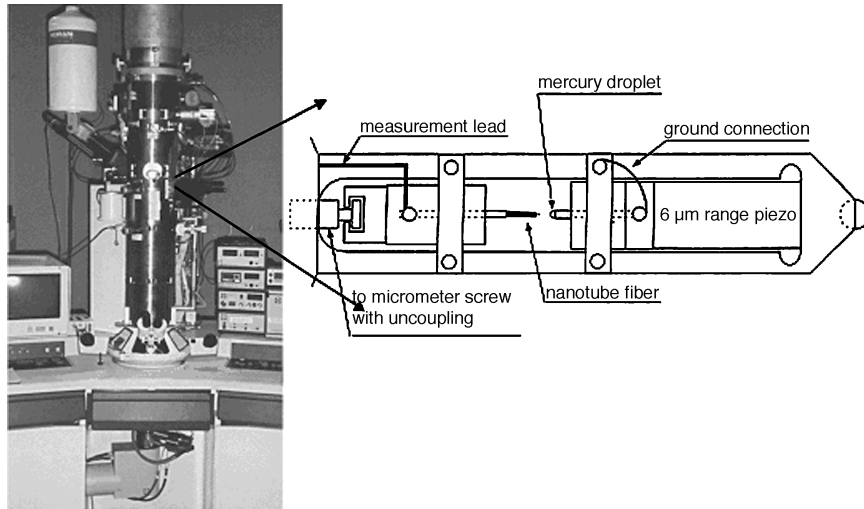
Fig. 1 A transmission electron microscope and a schematic diagram of a specimen holder for in situ measurements. (*View this art in color at www.dekker.com.*)

1–20 μm. The counter electrode is typically an Au ball of diameter ∼0.25 mm.

The Fundamental Resonance Frequency and Nonlinear Effect

Our first measurements were carried out for multiwalled carbon nanotubes produced by an arc-discharge technique. Because of the sharp needle shape of a carbon nanotube, it can be charged by an externally applied voltage; the induced charge is distributed mostly at the tip of the carbon nanotube and the electrostatic force results in the deflection of the nanotube. Alternatively, if an applied voltage is an alternating voltage, the charge on the tip of the nanotube is also oscillating, so is the force. If the applied frequency matches the natural resonance frequency of the nanotube, mechanical resonance is induced. By tuning the applied frequency, the first and the second harmonic resonances can be observed (Fig. 3). The analysis of the information provided by the resonance experiments relies on the theoretical model for the system. The most established theory for modeling mechanical systems is the continuous elasticity theory, which is valid for large-size objects. For atomic scale mechanics, we may have to rely on molecular dynamics. The diameter of the nanotube is between the continuous model and the atomistic model; thus we need to examine the validity of applying the classical elasticity theory for the data analysis.

We have compared the following three characteristics between the results predicted by the elasticity theory and the experimental results shown in Fig. 3. First, the theoretical node for the second harmonic resonance occurs at

$0.8L$, and the experiment showed ∼$0.76L$. Secondly, the frequency ratio between the second to the first mode is $v_2/v_2 = 6.27$ theoretically, while the observed one is $v_2/v_2 = 5.7$. The agreement is reasonably well if one looks into the assumptions made in the theoretical model: the nanotube is a uniform and homogeneous beam, and the
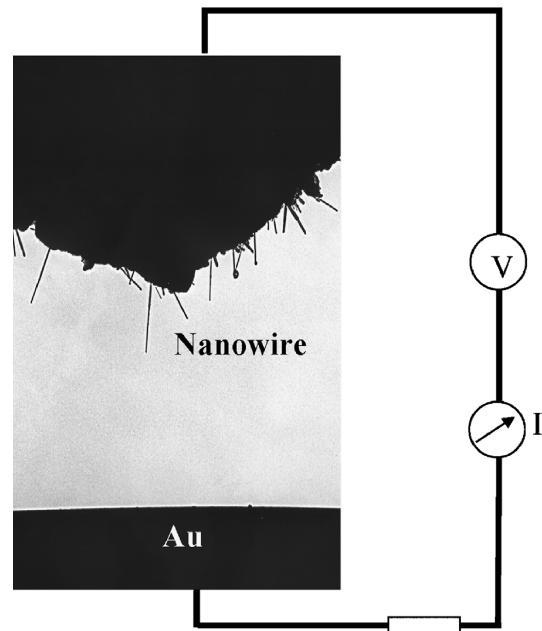

Fig. 2 TEM image showing one-dimensional nanostructures at the end of the electrode and the other counter electrode. A constant or alternating voltage can be applied to the two electrodes to induce electrostatic deflection or mechanical resonance.
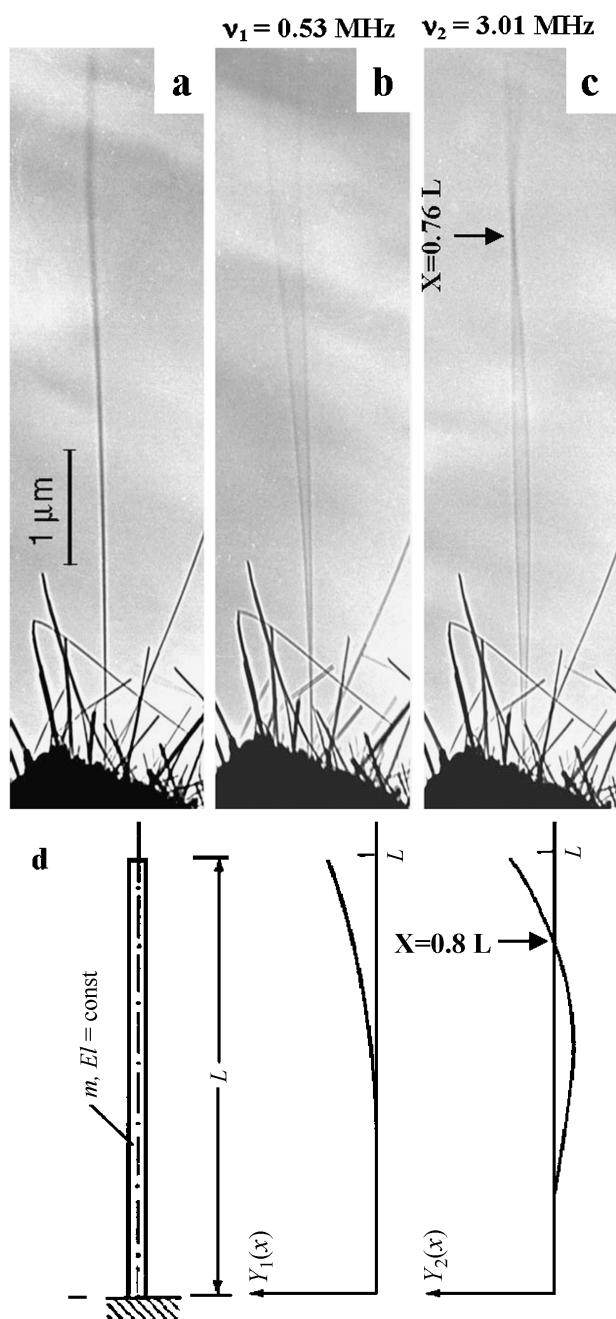
ORDER   REPRINTS

$\nu_1 = 0.53$ MHz $\nu_2 = 3.01$ MHz

Fig. 3 A selected carbon nanotube at (a) stationary, (b) the first harmonic resonance ($\nu_1 = 1.21$ MHz), and (c) the second harmonic resonance ($\nu_2 = 5.06$ MHz). (d) The traces of a uniform one-end fixed elastic beam at the first two resonance modes, as predicted by the continuous elasticity theory.

root of the clamping side is rigid. The latter, however, may not be realistic in practical experiment. Finally, the shape of the nanotube during resonance has been compared quantitatively with the shape calculated by the elasticity theory, and the agreement is excellent. Therefore we can still use the elasticity theory for the data analysis.

If the nanotube is approximated as a uniform solid bar with one end fixed on a substrate, from classical elasticity theory, the resonance frequency is given by[7]

$$v_i = \frac{\beta_i^2}{8\pi} \frac{1}{L^2} \sqrt{\frac{(D^2 + D_i^2)E_B}{\rho}} \tag{1}$$

where D is the tube outer diameter, D_i the inner diameter, L the length, ρ the density, and E_b the bending modulus. It must be pointed out that the bending modulus is different from Young's modulus, because bending modulus depends on the geometrical shape of the object. The resonance frequency is nanotube selective and it is a specific value of a nanotube.

The correlation between the applied frequency and the resonance frequency of the nanotube is not trivial. From Fig. 2 we know that there are some electrostatic charges built on the tip of the carbon nanotube. With consideration of the difference between the surface work functions between the carbon nanotube and the counter electrode (Au), a static charge exists even when the applied voltage is withdrawn. Therefore under an applied field the induced charge on the carbon nanotube can be represented by $Q = Q_o + \alpha V_o \cos\omega t$, where Q_o represents the charge on the tip to balance the difference in surface work functions, α is a geometrical factor, and V_o is the amplitude of the applied voltage. The force acting on the carbon nanotube is

$$\begin{aligned} F &= \beta(Q_o + \alpha V_o \cos \omega t)V_o \cos \omega t \\ &= \alpha\beta V_o^2/2 + \beta Q_o V_o \cos \omega t + \alpha\beta V_o^2/2 \cos 2\omega t \end{aligned} \tag{2}$$

where β is a proportional constant. Thus resonance can be induced at ω and 2ω at vibration amplitudes proportional to V_o and V_o^2, respectively. The former is a linear term in which the resonance frequency equals to the applied frequency, while the latter is a nonlinear term and the resonance frequency is twice of the applied frequency. In practical experiments, the linear and nonlinear terms can be distinguished by observing the dependence of the vibration amplitude on the magnitude of the voltage V_o. This is an important process to ensure the detection of the linear term.

Another factor that one needs to consider is to identify the true fundamental resonance frequency. From Eq. 1, the frequency ratio between the first two modes is 6.27. In practice, if resonance occurs at ω, resonance could occur also at 2ω, which is the double harmonic. To identify the fundamental frequency, one needs to examine the resonance at a frequency that is half or close to half of the observed resonance frequency; if no resonance occurs, the observed frequency is the true fundamental frequency.

The diameters of the tube can be directly determined from TEM images at a high accuracy. The determination
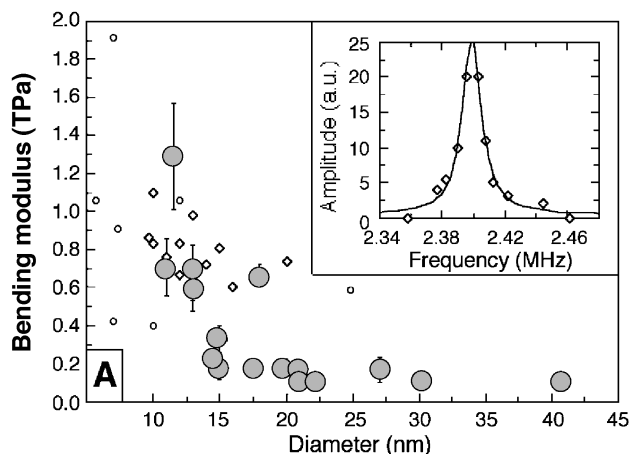
Fig. 4 Bending modulus of the multiwalled carbon nanotube produced by arc-discharge as a function of the outer diameter of the nanotube. The inner diameter of the nanotubes is ~5 nm, independent of the outer diameter. The FWHM of the resonance peak is inserted. (*View this art in color at www.dekker.com.*)

of length has to consider the 2-D projection effect of the tube. It is essential to tilt the tube and to catch its maximum length in TEM, which is likely to be the true length. This requires a TEM that gives a tilting angle as large as ±60°. Also, the operation voltage of the TEM is important to minimize radiation damage. The 100-kV TEM used in our experiments showed almost no detectable damage to a carbon nanotube, while a 200-kV electron could quickly damage a nanotube. The threshold for radiation damage of carbon nanotubes is ~150 kV.

To trace the sensitivity of resonance frequency on beam illumination and radiation damage at 100 kV, a carbon nanotube was resonanced for more than 30 min. The resonance frequency showed an increase of ~1.4% over the entire period of experiment, but no dependence on the electron dose was found. The FWHM for the resonance peak was measured to be $\Delta v/v = 0.6\%$ in a vacuum of 10^{-4}–10^{-5} Torr. A slight increase in the resonance frequency could be related to the change of carbon structure under the electron beam, but such an effect has a negligible effect on the measurement of the bending modulus.

The Young's modulus is a quantity that is defined to characterize the interatomic interaction force, and it is the double differential of the bonding energy curve between the two atoms. The ideal case is that it is an intrinsic property at the atomic level and is independent of the sample geometry. For the nanotube case, the bending of a nanotube is determined not only by the Young's modulus, but also by the geometrical shape of the nanotube, such as the wall thickness and tube diameter. What we have measured by the in situ TEM experiments is the bending modulus. Fig. 4 shows a group of experimentally measured bending modulus of multiwalled carbon nano-

tubes. It is apparent that the smaller-size nanotubes have a bending modulus approaching the Young's modulus, while the modulus for the larger-size ones is much smaller. This size-dependent property is related to the elastic deformation of the carbon nanotubes.

To explore the intrinsic meaning of the measured $\Delta v/v_1$ value, we consider a 1-D harmonic oscillator with an intrinsic resonance frequency v_1. If a viscosity (or friction) force is acting on the particle and the force is proportional to the instantaneous speed of the particle, the damping of the vibration amplitude is given by $\exp(-t/\tau_0)$, where τ_0 is the life decay constant of the oscillator. This decay constant is related to $\Delta v/v_1$ by $\Delta v/v_1 \ll 1$ by

$$\tau_0 = [(\Delta v/v_1)\pi v_1/1.732]^{-1} \tag{3}$$

For $\Delta v/v_1 = 0.65\%$, $v_1 = 1.0$ MHz, the lifetime is $\tau_0 = 85$ μsec. From the definition of τ_0, the viscosity/friction coefficient $\eta = 2M/\tau_0$, where M is the mass of the particle; thus the time decay constant depends mainly on the viscosity coefficient of the nanotube in vacuum (10^{-4} Torr) under which the measurement was made, and it is almost independent of the intrinsic structure of the carbon nanotube. This agrees with our experimental observation and Eq. 1 can also be used to explain the larger value of $\Delta v/v_1$ obtained in air than that in vacuum given that the atmosphere should have a higher viscosity (friction) coefficient.

Theoretical investigation by Liu et al.[8] suggests that the Eq. 1 used for the analysis is based on the linear analysis, which is valid for a small amplitude of vibration; for large vibration amplitude, the nonlinear analysis may have to be used. Based on the nonlinear elasticity theory, they have successfully explained the rippling effect observed experimentally by Wang et al.[4] In practical experiments, the resonance frequency shows no drift as the vibration increases to as large as 30°, suggesting that the frequency measured can still be quantified using the linear analysis.

BENDING MODULUS OF COMPOSITE NANOWIRES

The technique demonstrated for carbon nanotubes applies to any nanowire shape object regardless of its conductivity.[9] Here we use composite silicon carbide–silica nanowires synthesized by a solid–vapor process as an example. The as-synthesized materials are grouped into three basic nanowire structures: pure SiO_x nanowires, coaxially SiO_x sheathed β-SiC nanowires, and biaxial β-SiC–SiO_x nanowires. Fig. 5 depicts the TEM images of the nanowires and their cross-section images, showing the coaxial and biaxial structures. The nanowires are uniform with a diameter of 50–80 nm, and a length that can be as
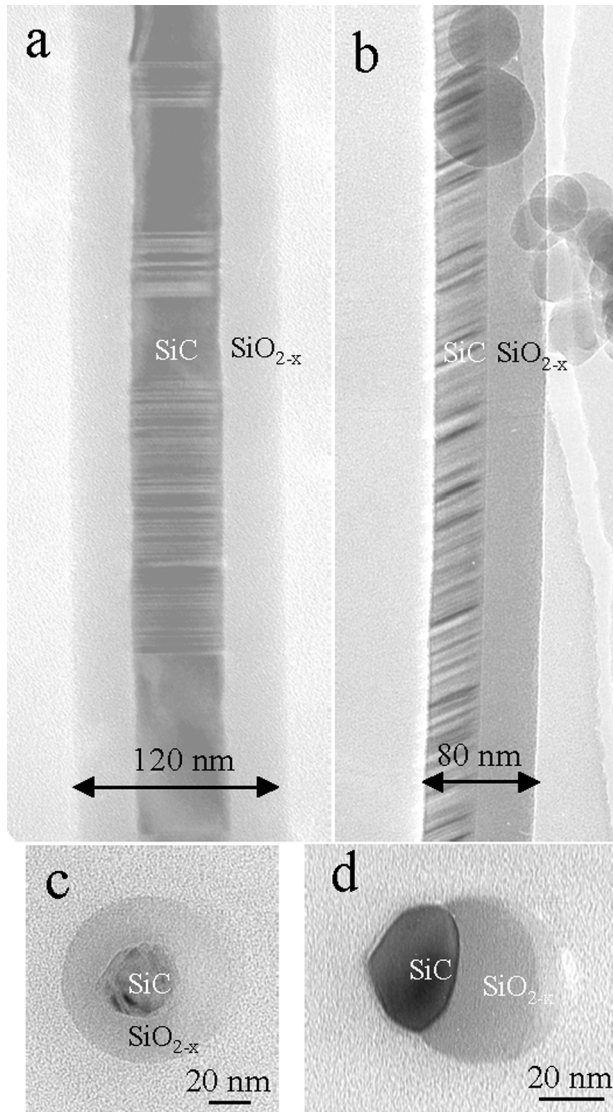
Fig. 5 (a,b) TEM images of the coaxial and biaxial structured SiC–SiO$_x$ nanowires, and (c,d) the cross-sectional TEM images, respectively.

long as 100 μm. The coaxial SiC–SiO$_x$ nanowires have been extensively studied and have a ⟨111⟩ growth direction with a high density of twins and stacking faults perpendicular to the growth direction.

For a beam with one end hinged and the other free, the resonance frequency is given by:[7]

$$v_0 = (\beta^2/2\pi)(EI/m)^{1/2}/L^2 \tag{4}$$

where v_o is the fundamental resonance frequency, $\beta = 1.875$, EI is the flexural rigidity (or bending stiffness), E is the Young's modulus, I is the moment of inertia about a particular axis of the rod, L is the length of the beam, and m is its mass per unit length. For a uniform solid beam with a coaxial cable structured nanowire whose core material density is ρ_c and diameter is D_c and a sheath material density that is ρ_s with outer diameter D_s, the average density of the nanowire is given by

$$\rho_e = \rho_c(D_c^2/D_s^2) + \rho_s(1 - D_c^2/D_s^2) \tag{5}$$

The effective Young's modulus of the composite nanowire, E_{eff}, is

$$E_{eff} = \rho_e[8\pi f_0 L^2/\beta^2 D_s]^2 \tag{6}$$

The bending modulus for the coaxial cable structured SiC–SiO$_x$ nanowires results in combination from SiC and SiO$_x$, where the contribution from the sheath layer of SiO$_x$ is more than that from the SiC core because of its larger flexural rigidity (or bending stiffness). The bending modulus increases as the diameter of the nanowire increases (Table 1), consistent with the theoretically expected values of $E_{eff} = \alpha E_{SiC} + (1 - \alpha)E_{Silica}$, where $\alpha = (D_c/D_s)^4$. The data match well to the calculated values for larger diameter nanowires.

From the cross-sectional TEM image of a biaxially structured nanowire, the outermost contour of the cross section of the nanowire can be approximated to be elliptical. Thus the effective Young's modulus of the nanowire can be calculated using Eq. 6 with the introduction of an effective moment of inertia and density. For an elliptical cross section of half long-axis a and half short-axis b, the moments of inertia are $I_x = \pi ab^3/4$, and $I_y = \pi ba^3/4$, where a and b can be calculated from the widths of the composite nanowire. With consideration of the equal probability of resonance with respect to the x and y axes, the effective moment of inertia introduced in the calculation is taken to be approximately $I = (I_x + I_y)/2$, and the density per unit length is $m_{eff} =$

Table 1 Measured Young's modulus of coaxial cable structured SiC–SiO$_x$ nanowires (SiC is the core, and silica is the sheath) ($\rho_{Silica} = 2.2 \times 10^3$ kg/m^3; $\rho_{SiC} = 3.2 \times 10^3$ kg/m^3). The Young's modulii of the bulk materials are $E_{SiC} = 466$ GPa and $E_{Silica} = 73$ GPa

D_s (nm) (±2 nm)	D_c (nm) (±1 nm)	L (μm) (±0.2 μm)	f_o (MHz)	E_{eff} (GPa) experimental	E_{eff} (GPa) theoretical
51	12.5	6.8	0.693	46±9.0	73
74	26	7.3	0.953	56±9.2	78
83	33	7.2	1.044	52±8.2	82
132	48	13.5	0.588	78±7.0	79
190	105	19.0	0.419	81±5.1	109

Table 2 Measured Young's modulus of biaxially structured SiC–SiO$_x$ nanowires. D_{wire} and D_{SiC} are the widths across the entire nanowire and across the SiC subnanowire, respectively

D_{wire} (nm) (±2 nm)	D_{SiC} (nm) (±1 nm)	L (μm) (±0.2 μm)	f_o (MHz)	E_{eff} (GPa) experimental
58	24	4.3	1.833	54±24.1
70	36	7.9	0.629	53±8.4
83	41	4.3	2.707	61±13.8
92	47	5.7	1.750	64±14.3

$A_{SiC}\rho_{SiC}+A_{Silica}\rho_{Silica}$, where A_{SiC} and A_{Silica} are the cross sectional areas of the SiC and SiO$_x$ sides, respectively. The experimentally measured Young's modulus is given in Table 2.

BENDING MODULUS OF OXIDE NANOBELTS

Nanobelts—Structurally Controlled Nanowires

In the literature, there are a few names being used for describing 1-D elongated structures, such as nanorod, nanowire, nanoribbon, nanofiber, and nanobelts. When we named the nanostructures to be ''nanobelts,''[10] we mean that the nanostructure has specific growth direction, the top/bottom surfaces and side surfaces are well-defined crystallographic facets. The requirements for nanowires are less restrictive than for nanobelts because a wire has a specific growth direction, but its side surfaces may not be well defined, and its cross section may not be uniform nor have a specific shape. Therefore, *we believe that nanobelts are more structurally controlled objects than nanowires, or simply a nanobelt is a nanowire that has well-defined side surfaces.* It is well known that the

physical property of a carbon nanotube is determined by the helical angle at which the graphite layer was rolled up. It is expected that, for thin nanobelts and nanowires, their physical and chemical properties will depend on the nature of the side surfaces.

The most typical nanobelt is ZnO (Fig. 6a), which has a distinct cross section from the nanotubes or nanowires.[10] Each nanobelt has a uniform width along its entire length, and the typical widths of the nanobelts are in the range of 50 to 300 nm. A ripple-like contrast appearing in the TEM image is due to the strain resulting from the bending of the belt. High-resolution TEM (HRTEM) and electron diffraction studies show that the ZnO nanobelts are structurally uniform, single crystalline, and dislocation free (Fig. 6b).

There are a few kinds of nanobelts that have been reported in the literature. Table 3 summarizes the nanobelt structures of function oxides.[10–14] Each type of nanobelts is defined by its crystallographic structure, the growth direction, top surfaces, and side surfaces. Some of the materials can grow along two directions, but they can be controlled experimentally. Although these materials belong to different crystallographic families, they do have a common faceted structure, which is the nanobelt structure. In addition, nanobelts of Cu(OH)$_2$,[15] MoO$_3$,[16,17] MgO,[18,19] and CuO.[20]
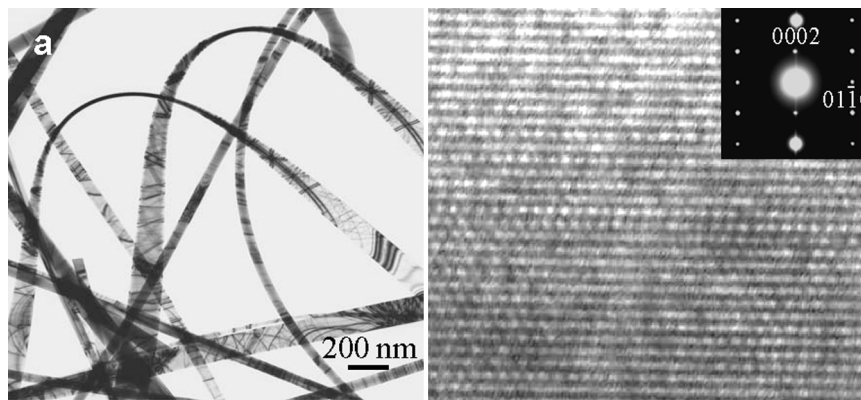

Fig. 6 (a) TEM image of ZnO nanobelts synthesized by a solid–vapor phase technique. (b) High-resolution TEM image of a ZnO nanobelt with incident electron beam direction along [2$\bar{1}$10]. The nanobelt grows along [0001], with top/bottom surfaces (2$\bar{1}$10) and side surfaces (01$\bar{1}$0).

Table 3 Crystallographic geometry of functional oxide nanobelts

Nanobelt	Crystal structure	Growth direction	Top surface	Side surface
ZnO	Wurtzite	[0001] or [01$\bar{1}$0]	±(2$\bar{1}\bar{1}$0) or ±(2$\bar{1}\bar{1}$0)	±(01$\bar{1}$0) or ±(0001)
Ga$_2$O$_3$	Monoclinic	[001] or [010]	±(100) or ±(100)	±(010) or ±(10$\bar{1}$)
t-SnO$_2$	Rutile	[101]	±(10$\bar{1}$)	±(010)
o-SnO$_2$ wire	Orthorhombic	[010]	±(100)	±(001)
In$_2$O$_3$	C-Rare earth	[001]	±(100)	±(010)
CdO	NaCl	[001]	±(100)	±(010)
PbO$_2$	Rutile	[010]	±(201)	±(10$\bar{1}$)

Dual-Mode Resonance of Nanobelts

Because of the mirror symmetry and rectangular cross section of the nanobelt (Fig. 7a), there are two distinct fundamental resonance frequencies corresponding to the vibration in the thickness and width directions, which are given from the classical elasticity theory as.[21]

$$v_x = \frac{\beta_1^2 T}{4\pi L^2} \sqrt{\frac{E_x}{3\rho}} \tag{7}$$

$$v_y = \frac{\beta_1^2 W}{4\pi L^2} \sqrt{\frac{E_y}{3\rho}} \tag{8}$$

where $\beta_1 = 1.875$; E_x and E_y are the bending modulus if the vibration is along the x axis (thickness direction)

and y direction (width direction), respectively; ρ is the density, L is the length, W is the width, and T is the thickness of the nanobelt. The two modes are decoupled and they can be observed separately in experiments.

Changing the frequency of the applied voltage, we found two fundamental frequencies in two orthogonal directions transverse to the nanobelt.[21] Fig. 7c and d shows the harmonic resonance with the vibration planes nearly perpendicular and parallel to the viewing direction, respectively. For calculating the bending modulus, it is critical to accurately measure the fundamental resonance frequency (v_1) and the dimensional sizes (L, and T and W) of the investigated ZnO nanobelts. To determine v_1, we have checked the stability of the resonance frequency to ensure that one end of the nanobelt is tightly fixed, and the resonant excitation has been carefully checked around the half value of the resonance frequency.
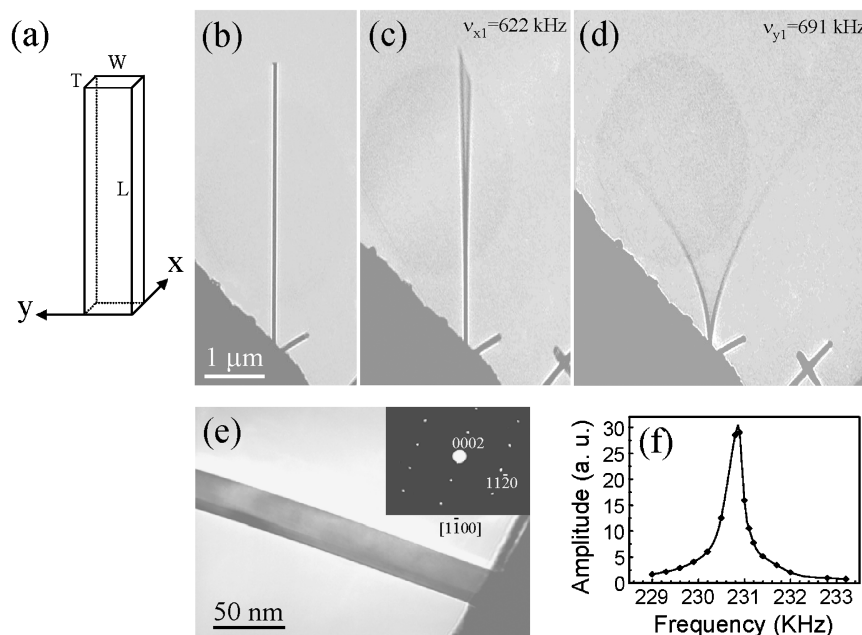

Fig. 7 A selected ZnO nanobelt at (a,b) stationary, (c) the first harmonic resonance in the x direction, $v_{x1}=622$ kHz, and (d) the first harmonic resonance in the y direction, $v_{y1}=691$ kHz. (e) An enlarged image of the nanobelt and its electron diffraction pattern (inset). The projected shape of the nanobelt is apparent. (f) The FWHM of the resonance peak measured from another ZnO nanobelt. The resonance occurs at 230.9 kHz.
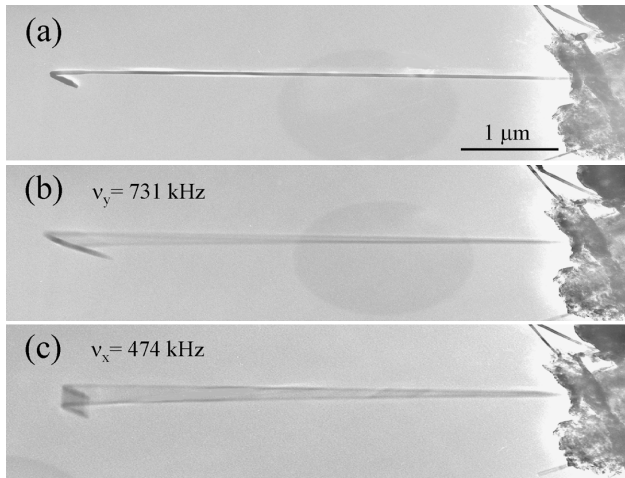
Fig. 8 A selected ZnO nanobelt with a hooked end at (a) stationary, (b) resonance at 731 kHz in the plane almost parallel to the viewing direction, and (c) resonance at 474 kHz in the place closely perpendicular to the viewing direction.

ZnO nanobelts can be used as a force sensor. Fig. 8a shows a selected ZnO nanobelt with a hooked end, which is equivalent to a cantilever with an integrated tip. Because of the two transverse vibration modes of the nanobelt, resonance along two orthogonal directions has been observed (Fig. 8b and c). The two resonance modes just correspond to the two modes of the tip operation when the nanobelt-base cantilever is used as a force sensor: one is the tapping mode and the other is the noncontact mode. Thus the force sensor fabricated using the ZnO nanobelts is versatile for applications on hard and soft surfaces.

Bending Modulus of Nanobelt

The geometrical parameters are the key for derivation of the mechanical property from the measured resonance frequencies. The specimen holder is rotated about its axis so that the nanobelt is aligned perpendicular to the electron beam; thus the real length (L) of the nanobelt can be obtained. The normal direction of the wide facet of the nanobelt could be firstly determined by electron diffraction pattern, which was $[2\bar{1}\bar{1}0]$ for the ZnO nanobelt. Then the nanobelt was tilted from its normal direction by rotating the specimen holder, and the tilting direction and angle were determined by the corresponding electron diffraction pattern. As shown in the inset of Fig. 7e, the electron beam direction is $[1\bar{1}00]$. The angle between $[1\bar{1}00]$ and $[2\bar{1}\bar{1}0]$ is 30°, i.e., the normal direction of the wide facet of this nanobelt is 30° tilted from the direction of the electron beam. Using the projected dimension measured from the TEM image (Fig. 7e), the geometrical parameters of this nanobelt are determined to be $W = 28$ nm and $T = 19$ nm. Based on the experimentally measured data, the bending modulus of the ZnO nanobelts is calculated using Eqs. 7 and 8. The experimental results are summarized in Table 4.[21] The bending modulus of the ZnO nanobelts was $\sim$52 GPa. This value represents the modulus that includes the scaling effect and geometrical shape, and it cannot be directly compared to the Young's modulus of ZnO ($c_{33} = 210$ GPa, $c_{13} = 104$ GPa),[22] because the shape of the nanobelt and the anisotropic structure of ZnO are convoluted in the measurement. The bending modulus measured by the resonance technique, however, has excellent agreement with the elastic modulus measured by nanoindentation for the same type of nanobelts.[23]

Although nanobelts of different sizes may have a slight difference in bending modulus, there is no obvious difference if the calculation was done using either Eq. 7 or Eq. 8. The ratio of two fundamental frequencies v_{y1}/v_{x1} is consistent with the aspect ratio W/T, as expected from Eqs. 7 and 8, because there is no significant difference between E_x and E_y.

The resonance technique demonstrated here is very sensitive to the structure of a nanowire. Fig. 9a and b shows a silicon nanowire that has a Au tip, but the Au

Table 4 Bending modulus of the ZnO nanobelts. E_x and E_y represents the bending modulus corresponding to the resonance along the thickness and width directions, respectively

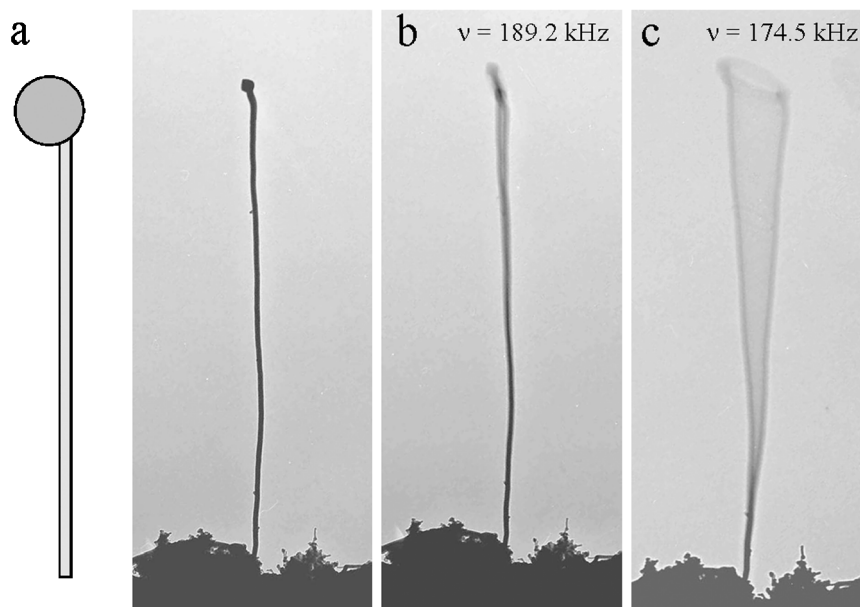| Nanobelt	Length L (μm) (±0.05)	Width W (nm) (±1)	Thickness T (nm) (±1)	Fundamental frequency (kHz)				Bending modulus (GPa)	
				W/T	v_{x1}	v_{y1}	v_{y1}/v_{x1}	E_x	E_y
1	8.25	55	33	1.7	232	373	1.6	46.6±0.6	50.1±0.6
2	4.73	28	19	1.5	396	576	1.4	44.3±1.3	45.5±2.9
3	4.07	31	20	1.6	662	958	1.4	56.3±0.9	64.6±2.3
4	8.90	44	39	1.1	210	231	1.1	37.9±0.6	39.9±1.2

Fig. 9 (a) A silicon nanowire with a gold particle at the tip, showing (b,c) two independent resonance along two perpendicular directions.

particle is off the symmetric axis of the nanowire. This asymmetric structure results in two distinct resonance along two perpendicular directions (Fig. 9c and d). The difference between the two resonance frequencies is related to the mass of the Au particle.

THE HARDNESS OF A NANOBELT BY NANOINDENTATION

Nanoscale mechanical properties of individual zinc oxide nanobelts were characterized by Nanoscope IIIa atomic
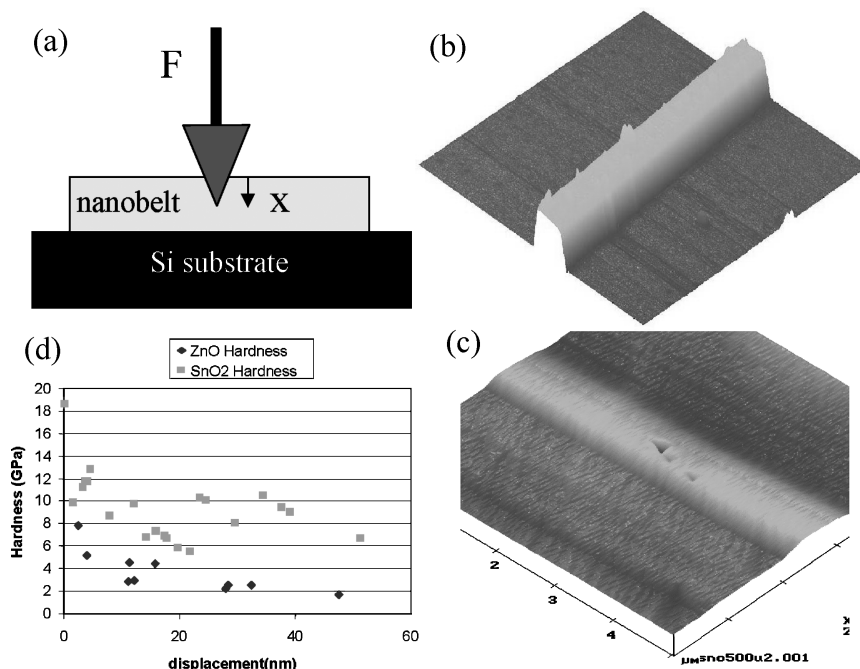
Fig. 10 (a) Schematic of nanoindentation on ZnO by AFM tip. (b,c) AFM image of a nanobelt before and after being indented, showing plastic deformation on the surfaces. (d) Hardness of ZnO and SnO$_2$ nanobelts as a function of penetration during nanoindentation. (*View this art in color at www.dekker.com.*)
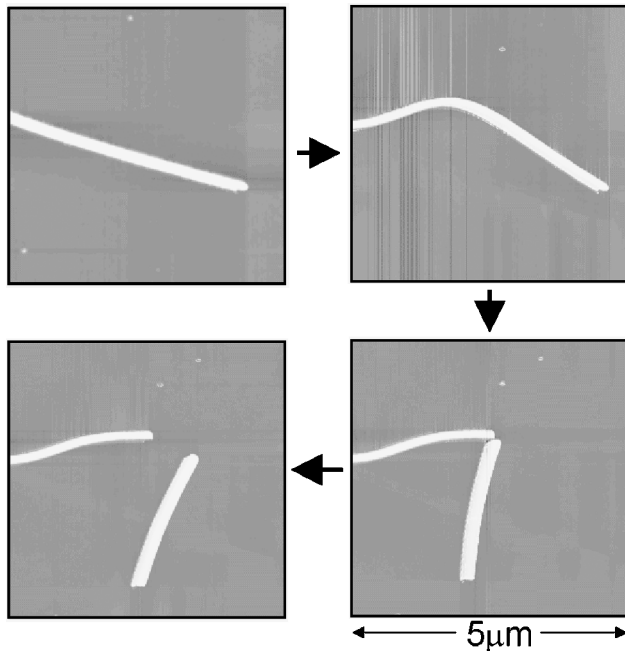
Fig. 11 A series of shape of a ZnO nanobelt created by manipulation using an AFM tip, showing deformation and break-up. (Image courtesy of M.S. Arnold, Ph. Avouris.) (*View this art in color at www.dekker.com.*)

force microscope (AFM) (Fig. 10a) and Hysitron Tribo-Scope with homemade side-view CCD camera.[23] The prepared nanobelt sample was investigated by two means: one is by tapping mode of Nanoscope IIIa, using a diamond indenter tip with a radius of <25 nm. The other is by STM mode of Hysitron TriboScope, an add-on force transducer from Hysitron Inc., using a diamond cubic corner tip with a radius of <40 nm. In either case, individual nanobelts were imaged, and then nanoindentations were made on the nanobelt using varied loads (Fig. 10b and c). After indentation, the indent was imaged in situ using the image mode of the AFM. For nanoindentations, the hardness is normally defined as the maximum load divided by the projected area of the indenter in contact with the sample at the maximum load. Thus,

$$H = \frac{P_{MAX}}{A_C} \tag{9}$$

where H, P_{MAX}, and A_C are the hardness, maximum applied load, and projected contact area at the maximum applied load, respectively. Because the indenter tip is not rigid during indentation, the elastic modulus cannot be directly determined from the load vs. the displacement curve. However, the reduced elastic modulus can be

determined from the unloading portion of the curve by the relation:

$$E_r = \frac{\sqrt{\pi}}{2} \cdot \frac{dP}{dh} \cdot \frac{1}{\sqrt{A_c}} \tag{10}$$

where E_r and dP/dh are the reduced modulus and experimentally measured stiffness, respectively.

Based on Eq. 9, using load vs. deflection curves during nanoindentation, the hardness of ZnO and SnO$_2$ nanobelts was calculated as a function of indentation penetration, and the result is summarized in Fig. 10d. The hardness of ZnO is lower than that in the SnO$_2$ nanobelt. Also, it can be seen that the lower the penetration of the nanoindentation, the higher the hardness of the nanobelt, which is attributed to the strain gradient effect (size effect) during nanoindentation for most materials.[24] The effective elastic modulus can also be derived from the force–displacement curve and the result is $E = 45$ GPa for ZnO, in good agreement with that from the resonance technique.[21]

NANOBELTS AS NANOCANTILEVERS

The cantilever-based scanning probe microscopy (SPM) technique is one of the most powerful approaches in imaging, manipulating, and measuring nanoscale properties and phenomena. The most conventional cantilever used for SPM is based on silicon, Si$_3$N$_4$ or SiC, which is fabricated by e-beam or optical lithography technique and typically has a dimension of thickness of ∼100 nm, width of ∼5 μm, and length of ∼50 μm. Utilization of nanowire- and nanotube-based cantilevers can have several advantages for SPM. Carbon nanotubes can be grown on the tip of a conventional cantilever and be used for imaging surfaces with a large degree of abrupt variation in surface morphology.[25,26] We demonstrate here the manipulation of nanobelts by AFM and its potential as nanocantilevers.[27]

Manipulation of nanobelts is important for integrating this structurally controlled nanomaterial with microelectrical mechanical system (MEMS). Using an AFM tip, a nanobelt can be manipulated into different shapes (Fig. 11). A ZnO nanobelt of 56 nm in width can be bent for over 60° without breaking, demonstrating extremely high mechanical flexibility. Further bending bent the nanobelt into two segments. This is a technique for cutting a nanobelt into specific length.

Combining MEMS technology with self-assembled nanobelts, we are able to produce cost-effective cantilevers with much heightened sensitivity for a range of
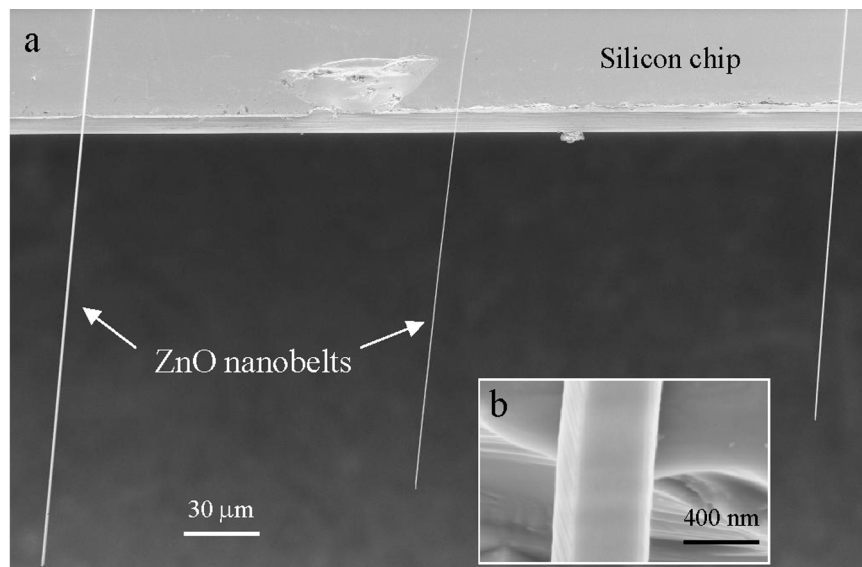
Fig. 12 Site-specific placement and alignment of ZnO nanobelts onto a silicon chip, forming nanocantilever arrays. The inset is an enlarged SEM image of the third nanocantilever showing its shape; the width of the cantilever was measured to be 525 nm.

devices and applications. Force, pressure, mass, thermal, biological, and chemical sensors are all prospective devices. Semiconducting nanobelts are ideal candidates for cantilever applications. Structurally, they are defect-free single crystals, providing excellent mechanical properties. The reduced dimensions of nanobelt cantilevers offer a significant increase in cantilever sensitivity. The cantilevers under consideration are simple in design and practice. Using a Dimension 3000 SPM in tapping mode, we have successfully lifted ZnO nanobelts from a silicon substrate. Capillary forces are responsible for the adhesion strength between the AFM probe and the ZnO nanobelts. Combining the aforementioned techniques with micromanipulation has led to the alignment of individual ZnO nanobelts onto silicon chips (Fig. 12). The aligned ZnO cantilevers were manipulated to have a range of lengths. This exemplifies our ability to tune the resonance frequency of each cantilever and thus modify cantilevers for different applications such as tapping and contact mode AFM. The nanobelt-based nanocantilever is ~50–1000 times smaller than the conventional cantilever. Decreased size in microoptical mechanical devices corresponds to increased sensitivity. Combining the aforementioned techniques with micromanipulation has led to the horizontal alignment of individual ZnO nanobelts onto silicon chips (Fig. 12). This exemplifies our ability to tune the resonance frequency of each cantilever and thus modify cantilevers for different applications such as contact, noncontact, and tapping mode AFM.

THE WORK FUNCTION AT THE TIP OF A NANOBELT BY RESONANCE TECHNIQUE

The field-emission property for well-aligned ZnO nanowire arrays has been reported,[28] demonstrating a promising application of semiconductor nanowires as field emitters for flat panel display. Following the Fowler–Nordheim (F–N) theory,[29] an important physical quantity in electron field emission is the surface work function, which is well documented for elemental materials. For the emitters such as ZnO nanowire arrays, most of the electrons are emitted from tips of the nanowires, and it is the local work function that matters to the properties of the field emission. However, the work function measured based on the F–N theory is an average over the large scale of emitting materials. So it is necessary to measure the local work function at the tip of an individual emitter. Gao et al.[30] have measured the work function at the tips of carbon nanotubes by an in situ TEM technique. The measurement relies on the mechanical resonance of the carbon nanotube induced by an externally applied oscillating voltage with tunable frequency.

The measurement of the work function at the tip of a single ZnO nanobelt was carried out in situ at 200 kV in a Hitachi HF-2000 FEG TEM. A specimen holder was built for applying a voltage across a nanobelt and its counter gold electrode. The nanobelts to be used for measurements are directly imaged under TEM. Fig. 13 is a setup for work function measurement. One end of the nanobelt was electrically attached to a gold wire, and the other end

faces directly against the gold ball. Because of the difference in the surface work function between the ZnO nanobelt and the counter Au ball, a static charge Q_0 exists at the tip of the nanobelt to balance this potential difference.[31] The magnitude of Q_0 is proportional to the difference between the work function of the nanobelt tip (NBT) and the Au electrode, $Q_0 = \alpha\,(\phi_{Au} - \phi_{NBT})$, where α is related to the geometry and distance between the nanobelt and the electrode.

The measurement is based on the mechanical resonance of the nanobelt induced by an externally alternative electric field. Experimentally, a constant voltage $V_{d.c.}$ and an oscillating voltage $V_{a.c.}\cos 2\pi ft$ are applied onto the nanobelt (Fig. 13a), where f is the frequency and $V_{a.c.}$ is the amplitude. Thus the total induced charge on the nanobelt is

$$Q = Q_0 + \alpha e(V_{d.c.} + V_{a.c.}\cos 2\pi ft) \tag{11}$$

The force acting on the nanobelt is proportional to the square of the total charge on the nanobelt

$$
\begin{aligned}
F &= \beta[Q_0 + \alpha e(V_{d.c.} + V_{a.c.}\cos 2\pi ft)]^2 \\
&= \alpha^2\beta\{[(\phi_{Au} - \phi_{NBT} + eV_{d.c.})^2 + e^2 V_{a.c.}^2/2] \\
&\quad + 2eV_{a.c.}(\phi_{Au} - \phi_{NBT} + eV_{d.c.}) \\
&\quad \times \cos 2\pi ft + e^2 V_{a.c.}^2/2 \cos 4\pi ft\}
\end{aligned}
\tag{12}
$$

where β is a proportional constant. In Eq. 12, the first term is constant and it causes a static deflection of the ZnO nanobelt. The second term is a linear term, and the res-
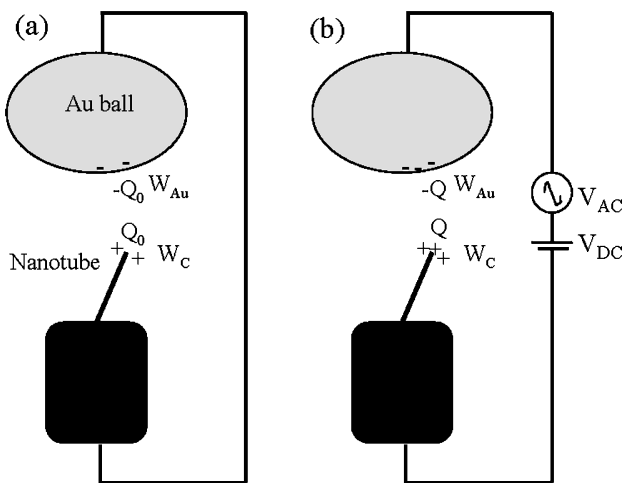
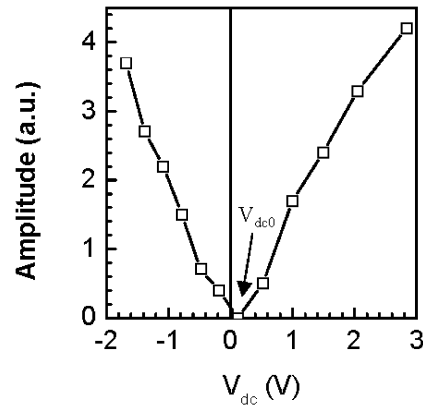**Fig. 13** Experimental set-up for measuring the work function at the tip of a ZnO nanobelt.

Fig. 14 A plot of vibration amplitude of a ZnO nanobelt as a function of the applied direct current voltage, from which the offset voltage $V_{dc0} = 0.12$ V.

onance occurs if the applied frequency f is tuned to the intrinsic mechanical resonance frequency f_0 of the ZnO nanobelt. The most important result of Eq. 12 is that, for the linear term, the resonance amplitude A of the nanobelt is proportional to $V_{a.c.}(\phi_{Au} - \phi_{NBT} + eV_{d.c.})$.

The principle of the measurement is as follows. We first set $V_{d.c.} = 0$ and tune the frequency f to get the mechanical resonance induced by the applied oscillating field. Second, under the resonance condition of keeping $f = f_0$ and $V_{a.c.}$ constant, slowly change the magnitude of $V_{d.c.}$ from zero to a value $V_{d.c.0}$ that satisfies $\phi_{Au} - \phi_{NBT} + eV_{d.c.0} = 0$. At this moment, the resonance amplitude A becomes zero although the external a.c. voltage is still in effect. Therefore the work function at the tip of the ZnO nanobelt is $\phi_{NBT} = \phi_{Au} + eV_{d.c.0}$, while $\phi_{Au} = 5.1$ eV. Fig. 14 is a plot of the vibration amplitude A of the nanobelt as a function of the applied direct current voltage $V_{d.c.}$, from which the value for $V_{d.c.0}$ is determined. The work function of the ZnO nanobelts is ~ 5.2 eV.[32]

CONCLUSION

The property characterization of nanomaterials is challenged by their small-size structures because of the difficulties in manipulation. A typical example is the mechanical properties of individual 1-D nanostructures, such as nanotubes, nanowires, and nanobelts. This chapter reviews the experimental methods for measuring the mechanical properties of 1-D nanostructures using a resonance technique in TEM. The static and dynamic properties of the 1-D nanostructures can be obtained by applying controllable static and alternating electric fields.

The resonance of carbon nanotubes can be induced by tuning the frequency of the applied voltage. The technique is powerful in such a way that it can directly correlate the atomic-scale microstructure of the carbon nanotube with its physical properties, providing a one-to-one correspondence in structure–property characterization.

Because of the rectangular cross section of the nanobelt, two fundamental resonance modes have been observed corresponding to two orthogonal transverse vibration directions, showing the versatile applications of nanobelts as nanocantilevers and nanoresonators. The bending modulus of the ZnO nanobelts was measured to be ~52 GPa. Nanobelts have also been demonstrated as ultrasmall nanocantilevers for sensor and possibly imaging applications in AFM.

ACKNOWLEDGMENTS

REFERENCES

1. Wang, Z.L.; Liu, Y.; Zhang, Z. *Handbook of Nanophase and Nanostructured Materials*; 2002; Vols. I–IV. Tsinghua University Press: Beijing; Kluwer Academic Publisher: New York.

2. Wang, Z.L.; Hui, C. *Electron Microscopy of Nanotubes*; Kluwer Academic Publisher: New York, 2003.

3. Poncharal, P.; Wang, Z.L.; Ugarte, D.; de Heer, W.A. Electrostatic deflections and electromechanical resonances of carbon nanotubes. Science **1999**, *283*, 1513–1516.

4. Wang, Z.L.; Poncharal, P.; de Heer, W.A. Nanomeasurements of individual carbon nanotubes by in-situ TEM. Pure Appl. Chem. **2000**, *72*, 209–219.

5. Gao, R.P.; Wang, Z.L.; Bai, Z.G.; de Heer, W.A.; Dai, L.M.; Gao, M. Nanomechanics of aligned carbon nanotube arrays. Phys. Rev. Lett. **2000**, *85*, 622–635.

6. Wang, Z.L.; Poncharal, P.; de Heer, W.A. Measuring physical and mechanical properties of individual carbon nanotubes by in-situ TEM. J. Phys. Chem. Solids **2000**, *61*, 1025–1030.

7. Meirovich, L. *Elements of Vibration Analysis*; McGraw-Hill: New York, 1986.

8. Liu, J.Z.; Zheng, Q.S.; Jiang, Q. Effect of ripping mode on resonances of carbon nanotubes. Phys. Rev. Lett. **2001**, *86*, 4843–4846.

9. Wang, Z.L.; Dai, Z.R.; Bai, Z.G.; Gao, R.P.; Gole, J.L. Side-by-side silicon carbide-silica biaxial nanowires: Synthesis, structure and mechanical properties. Appl. Phys. Lett. **2000**, *77*, 3349–3351.

10. Pan, Z.W.; Dai, Z.R.; Wang, Z.L. Nanobelts of semiconducting oxides. Science **2001**, *291*, 1947–1949.

11. Wang, Z.L.; Pan, Z.W.; Dai, Z.R. Semiconducting Oxide Nanostructures. US Patent No. 6,586,095, July 1, 2003.

12. Dai, Z.R.; Pan, Z.W.; Wang, Z.L. Gallium oxide nanoribbons and nanosheets. J. Phys. Chem., B **2002**, *106*, 902–904.

13. Dai, Z.R.; Pan, Z.W.; Wang, Z.L. Growth and structure evolution of novel tin oxide diskettes. J. Am. Chem. Soc. **2002**, *124*, 8673–8680.

14. Kong, X.Y.; Wang, Z.L. Spontaneous polarization and helical nanosprings of piezoelectric nanobelts. Nano Lett. **2003**, *in press*.

15. Wen, X.G.; Zhang, W.X.; Yang, S.H.; Dai, Z.R.; Wang, Z.L. Solution phase synthesis of Cu(OH)/sub 2/nanoribbons by coordination self-assembly using Cu/sub 2/S nanowires as precursors. Nano Lett. **2002**, *2* (12), 1397–1401.

16. Li, Y.B.; Bando, Y.; Golberg, D.; Kurashima, K. Field emission from MoO/sub 3/nanobelts. Appl. Phys. Lett. **2002**, *81* (26), 5048–5050.

17. Zhou, J.; Xu, N.S.; Deng, S.Z.; Chen, J.; She, J.C.; Wang, Z.L. Large-area nanowire arrays of molybdenum and molybdenum oxides: Synthesis and field emission properties. Adv. Mater. **2003**. *in press*.

18. Li, Y.B.; Bando, Y.; Sato, T. Preparation of network-like MgO nanobelts on Si substrate. Chem. Phys. Lett. **2002**, *359* (1–2), 141–145.

19. Liu, J.; Cai, J.; Son, Y.C.; Gao, Q.M.; Suib, S.L.; Aindow, M. Magnesium manganese oxide nanoribbons: Synthesis, characterization, and catalytic application. J. Phys. Chem., B **2002**, *106* (38), 9761.

20. Wen, X.G.; Zhang, W.X.; Yang, S.H. Synthesis of Cu- (OH)2 and CuO nanoribbon arrays on a copper surface. Langmuir **2003**, *19*, 5898–5903.

21. Bai, X.D.; Wang, E.G.; Gao, P.X.; Wang, Z.L. Dual-mode mechanical resonance of individual ZnO nanobelts. Appl. Phys. Lett. **2003**, *82*, 4806–4808.

22. Carlotti, G.; Socino, G.; Petri, A.; Verona, E. Acoustic investigation of the elastic properties of ZnO films. Appl. Phys. Lett. **1987**, *51*, 1889–1891.

23. Mao, S.X.; Zhao, M.H.; Wang, Z.L. Probing nano-scale mechanical properties of individual semiconducting nanobelt. Appl. Phys. Lett. **2002**, *83*, 993–995.

24. Duan, D.M.; Wu, N.; Slaughter, W.S.; Mao, S.X. Length scale effect on mechanical behavior due to strain gradient plasticity. Mater. Sci. Eng., A **2001**, *A303* (1–2), 241–249.

25. Yenilmez, E.; Wang, Q.; Chen, R.J.; Wang, D.; Dai, H.J. Wafer scale production of carbon nanotube scanning probe tips for atomic force microscopy. Appl. Phys. Lett. **2002**, *80* (12), 2225–2227.

26. Dai, H.J.; Hafner, J.H.; Rinzler, A.G.; Colbert, D.T.; Smalley, R.E. Nanotubes as nanoprobes in scanning probe microscopy. Nature **1996**, *384*, 147–150.

27. Hughes, W.; Wang, Z.L. Nanobelt as nanocantilever. Appl. Phys. Lett. **2003**, *82*, 2886–2888.

28. Lee, C.J.; Lee, T.J.; Lyu, S.C.; Zhang, Y.; Ruh, H.; Lee, H.J. Field emission from well-aligned zinc oxide nanowires grown at low temperature. Appl. Phys. Lett. **2002**, *81* (19), 3648–3650.

29. Fowler, R.H.; Nordherim, L.W. Electron emission in intense electric fields. Proc. R. Soc., Lond., A **1928**, *119* (781), 173.

30. Gao, R.P.; Pan, Z.W.; Wang, Z.L. Work function at the tips of multi-walled carbon nanotubes. Appl. Phys. Lett. **2001**, *78*, 1757–1759.

31. Kelvin, L. Philos. Mag. **1898**, *46*, 82.

32. Bai, X.D.; Wang, E.G.; Gao, P.X.; Wang, Z.L. Measuring the work function at a nanobelt tip and at a nanoparticle surface. Nano Lett. **2003**, *3*, 1147–1150.

Request Permission or Order Reprints Instantly!